Chemical Science

Check for updates

High performance layer-by-layer Pt₃Ni(Pt-skin)-modified Pd/C for the oxygen reduction reaction†

Jing-Fang Huang [ID]* and Po-Kai Tseng

Bimetallic Pt–Ni with Pt on the outermost layer and an innermost layer enriched in Ni, referred to as Pt₃Ni(Pt-skin), is a promising configuration of an electrocatalyst for the oxygen reduction reaction (ORR) in fuel cells. We prepare a core (Pd)/shell (Pt₃Ni(Pt-skin)) catalyst (Pt₃Ni(Pt-skin)/Pd/C) from Zn underpotential deposition (UPD) on a Ni UPD modified Pd/C catalyst, facilitating Pt atomic layer-by-layer growth on the Ni surface through the galvanic replacement process. Pt₃Ni(Pt-skin)/Pd/C shows the best ORR performance, with a Pt specific activity of 16.7 mA cm^{-2} and Pt mass activity of 14.2 A mg$_{Pt}^{-1}$, which are 90- and 156- fold improvements over commercial Pt/C catalysts. The Pt₃Ni(Pt-skin) structure effectively inhibits Ni leaching to improve the durability in two accelerated durability test modes mimicking the catalyst lifetime and start-up/shut-down cycles.

Introduction

Cathodic oxygen reduction reaction ORR electrocatalysts play a crucial role in fuel cell performance.[1–3] The Pt catalyzed ORR has sluggish kinetics and requires a high overpotential, causing lower Pt specific activity (j_{kPt}, the catalytic activity normalized by the Pt electrochemically active surface area (ECSA)) and Pt mass activity (i_{mPt}, the catalytic activity per Pt mass). The high cost and the low durability of Pt ORR electrocatalysts remain a challenge for the widespread commercialization of fuel cells.[4–18] Alloying Pt with another transition metal (Co, Ni, Fe, *etc.*) has attracted much attention in the design of advanced electrocatalysts, as this approach not only decreases the Pt content but also enhances the catalytic activity and durability.[8,19–23] These designs include core–shell structured nanoparticles (NPs),[24,25] as well as de-alloyed[26–28] and porous structured NPs.[6,26] The Pt alloys may tailor the electronic (affecting the Pt–OH bond energetics) and geometric structures (affecting the Pt–Pt bond distance and coordination number) to enhance the catalytic activity.[8] The highest recorded j_{kPt} values were achieved on single crystal surfaces or well-defined NPs with a specifically engineered facet structure and alloy composition. For example, Stamenkovic *et al.* found that single-crystal Pt₃Ni (111) with Pt-skin had a j_{kPt} value 10 times higher than the corresponding Pt (111) surface and 90 times higher than the commercial Pt/C catalysts used for the ORR.[8] Pt₃Ni octahedral NPs were shown to exhibit favorable microstructures for greatly enhanced activity in the ORR,[28–30] but were still limited by their

insufficient stability due to Ni leaching from the alloys and decreased ECSA from the agglomeration of the NPs during electrochemical cycling.[31] Core–shell NPs represent a multimetallic structure with tunable properties to enhance ORR catalytic activity.[32–38] A promising structure to optimize i_{mPt} and Pt utilization is a thin shell or skin layers of Pt or Pt alloys over a non-Pt NP core. As reported by Adzic *et al.*, Cu underpotential deposition (UPD) is used as a sacrificial coating on the core, followed by galvanic replacement (Gal) with noble metal ions for the final shell metal.[7,39–41] UPD-Gal is one of the most successful methods to specifically coat Pt monolayers on different metals, but the commonly used Cu UPD (Cu$_u$) limits the options of Pt coating substrates due to its high work function, Φ_{Cu} (~4.94 eV).[42] It is known that when the Φ of an electrodeposited metal, Φ_M, is lower than that of the substrate metal, Φ_S, UPD may occur at a potential more positive than the equilibrium potential. The Kolb–Gerischer equation, $\Delta E = 0.5\Delta\Phi$ (ΔE is the underpotential shift in V and $\Delta\Phi$ is $\Phi_M - \Phi_S$ of the electron in eV), has been used to evaluate the level of underpotential shift.[43] Despite numerous attempts to synthesize Pt alloying nanocatalysts with Pt-skin surfaces on transition metals,[28,44–50] it still remains a challenge to demonstrate their existence at the nanoscale. To resolve this issue, we attempted to improve the elegant UPD-Gal approach, also referred to as electrochemical atomic layer deposition (E-ALD) or electrochemical atomic layer epitaxy EC-ALE.[51,52] In UPD-Gal, the UPD adlayer enables a type of surface limited reaction (SLR). SLRs occur only at the substrate or deposit surface and specifically form an atomic layer or a monolayer coverage. The "atomic layer" refers to a coverage less than a monolayer, a monolayer being a unit of deposit coverage. Zn UPD (Zn$_u$) was used to replace the Cu$_u$ in the UPD-Gal due to its lower value of Φ_{Zn} (~3.95 eV) compared to Φ_{Cu},[42] and the more negative standard

Department of Chemistry, National Chung Hsing University, Taichung 402, Taiwan, Republic of China. E-mail: jfh@dragon.nchu.edu.tw

reduction potential, E^0 $(Zn^{2+}/Zn) = -0.76$ V.[53] The lower Φ_{Zn} makes Zn_u occur on a greater variety of substrates, particularly Ni. Zn_u can therefore replace many metals that are nobler than Zn in the Gal process thanks to its more negative E^0.

We report Zn_u assisted UPD-Gal (ZnUPD-Gal) in a Ni UPD (Ni_u) process of constructing a layer-by-layer Pt_3Ni(Pt-skin) thin layer on a carbon-supported Pd electrocatalyst (Pd_{20}/C) (20 wt% Pd on XC-72 Valcan carbon, E-TEK) (Pt_3Ni(Pt-skin)/Pd_{20}/C). The Pt_3Ni(Pt-skin) structure retains the advantages of the ultra-thin layer structure and the synergetic effects of the Ni sublayer. Pt_3-Ni(Pt-skin)/Pd_{20}/C possesses an ultra-high $j_{kPt} = 16.7$ mA cm^{-2} and $i_{mPt} = 14.2$ A mg$_{Pt}^{-1}$ (Pt loading $= 2.97$ μg$_{Pt}$ cm^{-2}), at 0.9 V vs. RHE, which are 90-fold and 156-fold improvements, respectively, over commercial Pt/C catalysts (0.185 mA cm^{-2} and 0.091 A mg$_{Pt}^{-1}$, Pt loading $= 24$ μg$_{Pt}$ cm^{-2}). We also show that the perfect Pt_3Ni(Pt-skin) structure effectively inhibits Ni leaching, significantly improving the durability of catalysts.

Results and discussion

Fig. 1 shows the CVs of Ni_u and Zn_u on $Pd_{20}/C@GC$ in an Ar-saturated 0.5 M Na_2SO_4 aqueous solution (Na_2SO_{4aq}). These
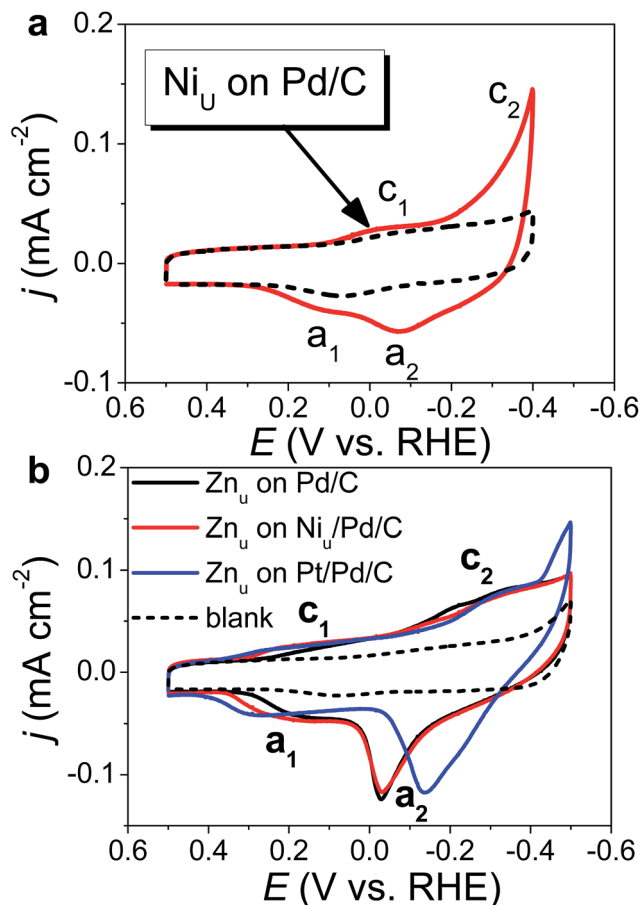
Fig. 1 CVs of (a) Ni_u on $Pd_{20}/C@GC$ and (b) Zn_u on $Pd_{20}/C@GC$, $Ni_u/Pd_{20}/C@GC$, and $Ni_u/Pd_{20}/C@GC$ recorded in Ar saturated 0.5 M Na_2SO_{4aq} (solid line) with and (dashed line) without (a) 20 mM $NiSO_4$ and (b) 20 mM $Zn(ClO_4)_2$ at a sweep rate of 50 mV s^{-1}.

voltammograms both show two pairs of redox waves, c_1/a_1 and c_2/a_2, which correspond to UPD/stripping and bulk deposition (OPD)/bulk stripping, respectively. These indicate that Ni_u or Zn_u can modify the Pd surface through controlled potential electrodeposition. Herein Zn_u was used to assist in the selective growth of Pt atomic layers on a given metallic surface, here Ni and Pt. Zn_u was further studied on $Ni_u/Pd_{20}/C@GC$ and Pt atomic layer covered $Pd_{20}/C@GC$ (Pt/$Pd_{20}/C@GC$) (Fig. 1b). $Ni_u/Pd_{20}/C$ was from direct electrodeposition of Ni_u on Pd_{20}/C in 0.5 M Na_2SO_{4aq} containing 20 mM $NiSO_4$. Pt/Pd_{20}/C was prepared by UPD-Gal to deposit a Pt atomic layer on Pd_{20}/C. The Zn_u redox waves, c_1/a_1, on Pd_{20}/C positively shifted from ~0.18 V to ~0.2 V and ~0.3 V after the modification of the Ni_u and Pt layer, respectively. The changes in CVs are ascribed to Zn_u and are surface dependent. Although Zn_u on Pt has been reported in the literature,[54] Zn_u on Ni has not been observed until now as the Ni_u was freshly produced without serious oxide or hydroxide surface inhibitors. The Zn_u on Pd, Ni, and Pt surfaces is related to the higher Φ_S of these substrates, Φ_{Pd} (~5.0 eV), Φ_{Ni} (~4.91 eV) and Φ_{Pt} (~5.4 eV), in comparison with the lower Φ_{Zn} (~3.95 eV).[42] Based on the Kolb–Gerischer equation, we could approximately calculate ΔE for the metal couples, Pd substrate/Zn, Ni substrate/Zn and Pt substrate/Zn, as ~0.53 V, ~0.48 V and ~0.7 V, respectively. This provides grounds for realizing that Zn_u on Pd, Ni and Pt is possible. In comparison, Cu_u cannot occur on Ni surfaces due to Φ_{Cu} (~4.94 eV) being close to Φ_{Ni}. This implies that Zn_u is a more suitable candidate to promote the Pt atomic layer to specifically form on a Ni surface.

Based on the findings of Zn_u on Ni, Pd and Pt surfaces and Ni_u on Pd and Pt surfaces, ZnUPD-Gal was used to prepare a Pt_3Ni(Pt-skin)/Pd_{20}/C electrocatalyst (Scheme 1). First, Ni_u was electrodeposited on the Pd surface of Pd_{20}/C, followed by modification of Zn_u on $Ni_u/Pd_{20}/C$. Subsequently, Zn_u was replaced by Pt in the Gal process, leading to Pt atomic layer covered $Ni_u/Pd_{20}/C$ (PtNi/Pd_{20}/C). The repetitive ZnUPD-Gal continually introduced the second and the third Pt atomic layers onto PtNi/Pd_{20}/C to obtain the desired electrocatalyst, Pt_3Ni(Pt-skin)/Pd_{20}/C. The micromorphology and elemental composition distribution of Pt_3Ni(Pt-skin)/Pd_{20}/C were examined by high-resolution transmission electron microscopy (HRTEM) combined with energy dispersive X-ray spectroscopy
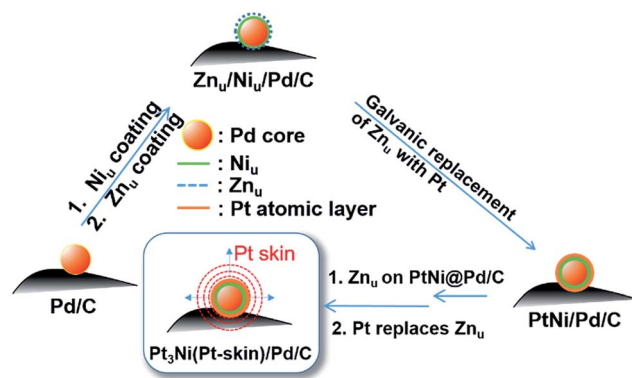
Scheme 1 The preparation process of Pt_3Ni(Pt-skin)/Pd_{20}/C electrocatalysts through ZnUPD-Gal on Ni_u.

(EDS) (Fig. 2a and b and S1†). In Fig. S1a–c,† typical bright-field TEM images of pristine Pd_{20}/C reveal a relatively uniform dispersion of Pd NP (Pd_{nano}) with sizes of approximately 4.8–5.6 nm (diameter). After Pt_3Ni(Pt-skin) modification, the growth of the particle size occurred as expected (diameter increased to ~6.8 nm) (Fig. S1d–f†). The core of Pt_3Ni(Pt-skin)/Pd_{nano} shows clear fringe orientations of the Pd (111) single-crystal structure (Fig. 2a). The EDS line profile analysis shows the distribution of Pt, Ni, and Pd components in a single NP (Fig. 2b). The width of Pt_3Ni(Pt-skin)/Pd_{nano} examined was 4 nm, as designated by the red line in Fig. 2a. The line profile analysis validates the core–shell structure, which is a Pd core covered by an ultra-thin PtNi shell with a thickness of approximately 1.2 nm. The Pd composition is constant and high in the particle center, and decreases from the edge of the core to the particle surface. Most of the Ni component is located at the interface between the Pd core and PtNi shell. At the exterior of the PtNi shell, the Pt intensity is approximately 2.5 times that of Ni in the interior of the PtNi shell. This analysis demonstrates the formation of a core (Pd)/shell (Pt_3Ni(Pt-skin)) structure. To extend the diversity of the ZnUPD-Gal with the Ni_u process, a three repeated PtNi layer covered Pd core (($PtNi)_3/Pd_{20}/C$) was also prepared as a control example. The EDS line profile analysis of $(PtNi)_3/Pd_{20}/C$ confirms that a Pd core/$(PtNi)_3$ shell structure was successfully obtained using this process (Fig. S2 and S3†).

The CVs of H_2SO_{4aq} were used to track different modified layers grown on the Pd surface. The typical CV of Pd_{20}/C shows redox peaks corresponding to the formation and removal of Pd hydroxide ($Pd(OH)_x$) (0.6–1.0 V vs. RHE) and H absorption (H_{ab})/desorption (0.3–0.0 V vs. RHE) (Fig. 3a). In comparison with the CV of pristine Pd_{20}/C, the first modified layer, Ni_u, on Pd_{20}/C inhibits the formation of $Pd(OH)_x$ and H_{ab}, causing the reduction of related redox charges on $Ni_u/Pd_{20}/C$. The following Pt atomic layers were grown in turn on the Ni_u surface by ZnUPD-Gal. With the increase of the Pt layer, characteristic Pt redox
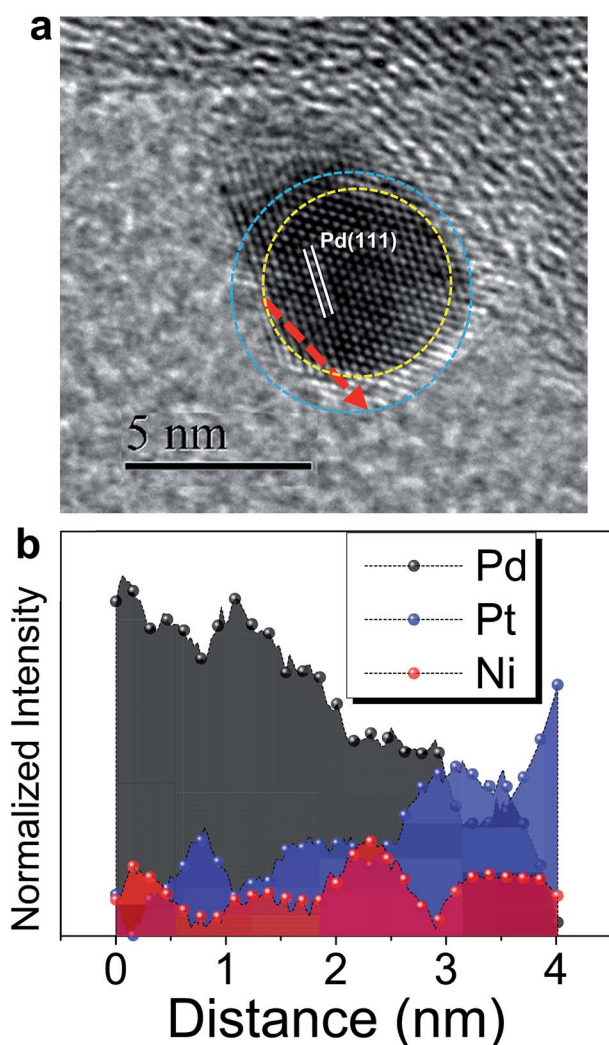
Fig. 2 (a) The representative HRTEM image of a core (Pd)/shell (Pt_3Ni(Pt-skin)) nanoparticle; (b) the corresponding EDS line-scan profile along the red dashed line as shown in (a).
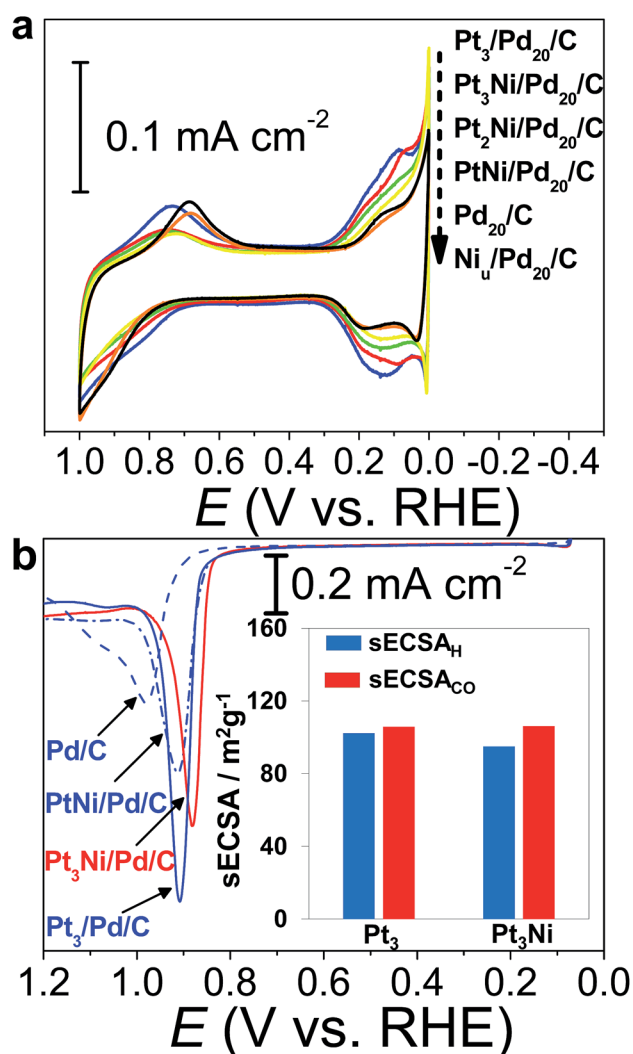
Fig. 3 Electrochemical surface characterization of electrocatalysts by using a GC electrode in 0.1 M H_2SO_{4aq}: (a) cyclic voltammograms of (blue) $Pt_3/Pd_{20}/C$, (red) Pt_3Ni(Pt-skin)/Pd_{20}/C, (green) Pt_2Ni(Pt-skin)/Pd_{20}/C, (yellow) $PtNi$(Pt-skin)/Pd_{20}/C, (black) Pd_{20}/C, and (orange) $Ni_u/Pd_{20}/C$; (b) CO stripping curves. The inset shows (blue) $sECSA_H$ and (red) $sECSA_{CO}$ for (Pt_3) $Pt_3/Pd_{20}/C$ and (Pt_3Ni) Pt_3Ni(Pt-skin)/Pd_{20}/C.

waves, including the formation of Pt hydroxide $(Pt(OH)_x)$ occurred at a more negative potential ($\sim$0.75 V $vs.$ RHE) and hydrogen adsorption (H_{ad})/desorption waves gradually grew. For the purpose of comparison, three Pt layer-covered Pd_{20}/C@GC (Pt_3/Pd_{20}/C@GC) without Ni_u was also prepared using UPD-Gal. This indicated that the surface of Pt_3/Pd_{20}/C was mainly composed of Pt, due to the similar CV features of Pt_3/Pd_{20}/C and Pt/C. In comparison to the CV features of Pt_3/Pd_{20}/C, those of Pt_3Ni(Pt-skin)/Pd_{20}/C based on the same Pt content showed that the onset potential of H_{ad} shifted towards a more negative potential and the formation of $Pt(OH)_x$ occurred at a more positive potential. This is a consequence of the electronically modified structure of Pt for "Pt skin" surfaces by the subsurface Ni atoms, which leads to weakened interactions between Pt and adsorbates such as H_{ad} and surface hydroxides (OH_{ad}). This is also typical for the Pt_3Ni(Pt-skin) structure.[8,55] The H_{ad} integrated charge is a conventional approach in the estimation of ECSA ($ECSA_H$).[56] However, the suppression of H_{ad} on the Pt_3Ni(Pt-skin) structure can substantially affect the accurate estimation of the real ECSA. The electro-oxidation of adsorbed carbon monoxide (CO_{ad}), known as CO stripping, has been suggested as a complementary ECSA evaluation method $(ECSA_{CO})$.[55,57] Fig. 3b shows the voltammetric curves of CO stripping obtained for pristine Pd_{20}/C, $PtNi/Pd_{20}$/C, and Pt_3-Ni(Pt-skin)/Pd_{20}/C. The oxidation of the CO_{ad} takes place in a single peak whose peak potential shifts towards more negative values as the Pt content increases. The broad CO stripping peak for Pd_{20}/C becomes sharper with increasing Pt content in the PtNi shell.[58] These results suggest that the PtNi shell significantly weakens the interaction of Pd surface atoms with CO_{ad}. Interestingly, the onset of CO stripping on Pt_3Ni(Pt-skin)/Pd_{20}/C is more negatively shifted than on Pt_3/Pd/C, and the shape of the stripping peak is broader due to the weaker interaction of the Pt surface atoms with CO from the Ni sublayer. However, the similar charge of CO oxidation points to an equal coverage of CO. The specific ECSA ($sECSA = ECSA/$metal loading, $m^2\ g^{-1}$) for Pt_3Ni/Pd/C and Pt_3/Pd/C electrocatalysts was evaluated from $ECSA_H$ ($sECSA_H$) and $ECSA_{CO}$ ($sECSA_{CO}$), respectively (Fig. 3b). Although the suppression of $sECSA_H$ on Pt_3Ni/Pd/C (95.1 $m^2\ g^{-1}$) was observed in comparison with that of Pt_3/Pd/C (102.3 $m^2\ g^{-1}$), $sECSA_{CO}$ shows a similar value of $\sim$106 $m^2\ g^{-1}$ on both Pt_3Ni(Pt-skin)/Pd/C and Pt_3/Pd/C.

The ORR polarization curves were obtained with Pd_{20}/C, Ni/Pd_{20}/C, Pt_3/Pd_{20}/C, $PtNi/Pd_{20}$/C and Pt_3Ni(Pt-skin)/Pd_{20}/C electrocatalysts as thin films on the GC disc electrode of a RRDE in an O_2-saturated 0.1 M $HClO_4$ solution at 1600 rpm (Fig. 4a). The Pt ring electrode of the RRDE was potentiostated at 1.1 V to collect the ring current (i_r) related to the H_2O_2 oxidation reaction. The polarization curves on the disc electrode displayed two distinguishable potential regions: well-defined diffusion limiting currents (i_D) for the ORR below 0.7 V and a mixed kinetic-diffusion control region between 0.7 and 1.1 V. In both potential regions, i_r was a rather small fraction of i_D for all electrocatalysts, revealing that the ORR proceeds almost entirely through the $4e^-$ reduction pathway. A quantitative presentation of the H_2O_2 production (current efficiency, $\chi_{H_2O_2}$) was given using eqn (1):[20]
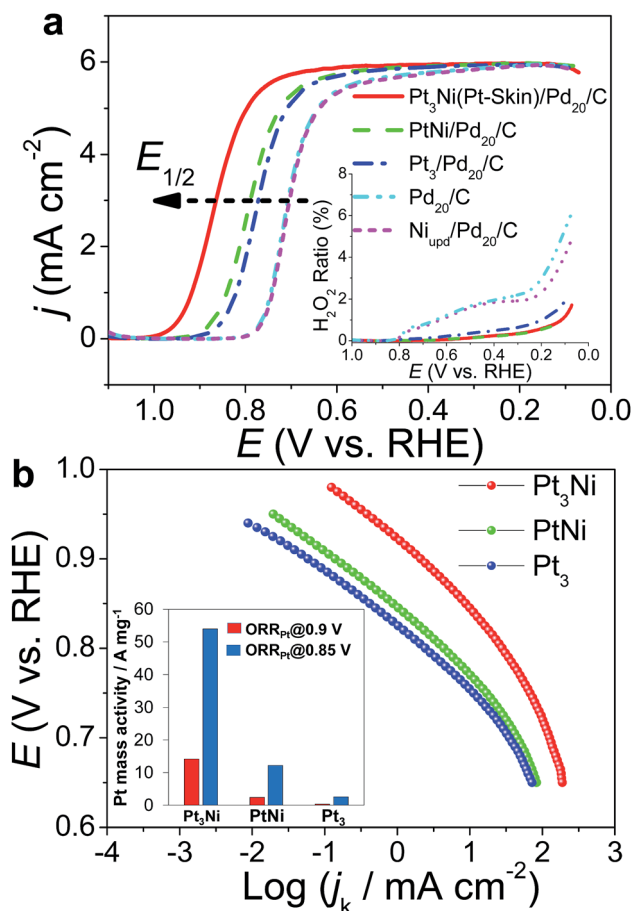

Fig. 4 (a) ORR polarization curves of Pt_3Ni(Pt-skin)/Pd_{20}/C, $PtNi/Pd_{20}$/C, Pt_3/Pd_{20}/C, Ni_u/Pd_{20}/C, and commercial Pd_{20}/C catalysts recorded at room temperature in an O_2-saturated 0.1 M $HClO_4$ aqueous solution with a scan rate of 10 mV s^{-1} and a rotation rate of 1600 rpm. Inset: the corresponding H_2O_2 production current efficiency, $\chi_{H_2O_2}$, from ring current (i_r) during the ORR, ring potential = 1.1 V, collection efficiency: $N = 0.2$. (b) The corresponding Tafel plots. Inset: (ORR@0.85 V and ORR@0.9 V) mass activities and (ORR$_{Pt}$@0.85 V and ORR$_{Pt}$@0.9 V) Pt mass activities for (Pt_3Ni) Pt_3Ni(Pt-skin)/Pd_{20}/C, ($PtNi$) $PtNi/Pd_{20}$/C, and (Pt_3) Pt_3/Pd_{20}/C measured at 0.85 V and 0.9 V.

$$\chi_{H_2O_2} = \frac{2i_r/N}{i_D + i_r/N} \qquad (1)$$

where N is the collection efficiency of the RRDE. In the potential region of $0.05 < E < 1$ V, similarly small amounts of H_2O_2 were detected on the ring electrode from the Pd_{20}/C and Ni_u/Pd_{20}/C electrocatalysts, implying that Ni modification does not alter the reaction pathways. Pt-containing shells on the other three electrocatalysts (Pt_3/Pd_{20}/C, $PtNi/Pd_{20}$/C and Pt_3Ni(Pt-skin)/Pd_{20}/C) effectively inhibited the production of H_2O_2 during the ORR, since there was no detectable H_2O_2 on the ring electrode in the kinetically controlled potential region, implying that Pt atomic layers perfectly covered the outermost layer of Pt-containing shells. The half-wave potential of an ORR polarization curve, $E_{1/2}$, is often used to evaluate the electrocatalytic activity of a catalyst. $E_{1/2}$ increased in the following sequence: Pd_{20}/C $\sim$ Ni_u/Pd_{20}/C $<$ Pt_3/Pd_{20}/C $<$ $PtNi/Pd_{20}$/C $\ll$ Pt_3Ni(Pt-skin)/Pd_{20}/C. Pt_3Ni(Pt-skin)/Pd_{20}/C showed a marked positive shift in $E_{1/2}$ of 200 mV and 100 mV relative to Pd_{20}/C and

$Pt_3/Pd_{20}/C$, respectively. These data show that the Pt_3Ni(Pt-skin) structure exhibits marked activity improvements over Pd_{20}/C and $Pt_3/Pd_{20}/C$ catalysts. Fig. 4b compares the Tafel plots for the specific activity (j_k) towards the ORR obtained by normalizing the kinetic current (i_k) to the $ECSA_{CO}$ for $Pt_3/Pd_{20}/C$, $PtNi/Pd_{20}/C$ and Pt_3Ni(Pt-skin)/Pd_{20}/C, at 1600 rpm in the cathodic sweep direction. i_k was obtained from the measured currents, corrected for mass transport according to eqn (2).[59–61]

$$\frac{1}{i} = \frac{1}{i_k} + \frac{1}{i_D} \qquad (2)$$

Two Tafel slopes of $Pt_3/Pd_{20}/C$, $-60/-119$ mV dec^{-1}, were similar to those observed on conventional Pt/C. The values of the Tafel slopes of Pt_3Ni(Pt-skin)/Pd_{20}/C, $-70/-122$ mV dec^{-1}, showed a slight difference from those of $Pt_3/Pd_{20}/C$, probably owing to a different state and coverage of $Pt(OH)_x$ after the insertion of the Ni sublayer. When comparing j_k for different electrocatalysts at 0.9 V, the specific activity of Pt_3Ni(Pt-skin)/Pd_{20}/C was 2.34 mA cm^{-2}, which is much higher than those of $Pt_3/Pd_{20}/C$ (~0.06 mA cm^{-2}) and $PtNi/Pd_{20}/C$ (~0.16 mA cm^{-2}). Considering the $ECSA_{CO}$ contribution from Pt ($ECSA_{CO(Pt)}$ = $sECSA_{CO}$ × the mass of Pt (~2.97 μg_{Pt} cm^{-2})), Pt_3Ni(Pt-skin)/Pd_{20}/C shows a very high specific activity j_k of Pt (j_{kPt}) 16.7 mA cm^{-2} at 0.9 V, which is 90-fold enhancement over commercial Pt/C catalysts (0.185 mA cm^{-2}, Pt loading = 24 μg cm^{-2}) and even higher than the possibly highest record, 10.3 mA cm^{-2}, for octahedral Mo–Pt_3Ni/C (the particle shape is close to spherical)[62] and 11.5 mA cm^{-2}, for jagged Pt nanowires from de-alloying PtNi nanowires with a totally different microstructure.[31] The Pt content was obtained by measuring the charge associated with Zn_u (after correcting for the double layer charging) on Pd_{20}/C and assuming that there was a one-to-one ratio between the UPD adlayer and the Pt atoms. The total amount of Pt on $Pt_3/Pd_{20}/C$ and Pt_3Ni(Pt-skin)/Pd_{20}/C (~2.97 μg_{Pt} cm^{-2}) was much less than that on the commercial Pt/C (~24 μg_{Pt} cm^{-2}). This finding highlights the advantages of ultra-thin layer electrocatalysts, which contribute to not only the reduction of Pt content but also the enhancement of catalytic activity thanks to their high Pt utilization.[39,40] The Pt mass activities (i_{mPt}) at 0.9 and 0.85 V were calculated based on the ORR polarization curves and the amount of Pt on the electrodes. The Pt_3Ni(Pt-skin) structure retained the advantages of the ultra-thin layer structure and the synergetic effect of the Ni sublayer presented an ultra-high i_{mPt} of 14.2 A mg$_{Pt}^{-1}$ based on Pt loading (2.97 μg_{Pt} cm^{-2}) at 0.9 V. The i_{mPt} of the Pt_3Ni(Pt-

skin)/Pd_{20}/C catalyst achieved a 37- and 156-fold improvement over $Pt_3/Pd_{20}/C$ (0.381 A mg$_{Pt}^{-1}$, ~2.97 μg_{Pt} cm^{-2}) and commercial Pt/C catalysts (0.091 A mg$_{Pt}^{-1}$, ~24 μg_{Pt} cm^{-2}), respectively. The i_{mPt} is more than an order of magnitude greater than the U.S. Department of Energy's 2017 goal (0.44 A mg$_{Pt}^{-1}$). The i_{mPt} of Pt_3Ni(Pt-skin)/Pd_{20}/C is even higher than those of the state-of-the-art Pt–Ni catalysts, including the recently reported PtNi nanoframe catalysts (5.7 A mg$_{Pt}^{-1}$),[28] Mo–Pt_3Ni/C (6.98 A mg$_{Pt}^{-1}$, Pt loading = 4.08 μg_{Pt} cm^{-2})[62] and jagged Pt nanowires (13.6 A mg$_{Pt}^{-1}$, Pt loading = 2.2 μg_{Pt} cm^{-2}) (Table 1).[31] Two accelerated durability test (ADT) modes further examined the Pt_3Ni(Pt-skin)/Pd_{20}/C lifetime (Fig. 5).

One was a commonly used test mode (ADT$_s$) which applied a linear potential sweep from 0.6 to 1.0 V vs. RHE at a scan rate of 50 mV s^{-1} for 20 000 cycles in O$_2$-saturated 0.1 M HClO$_4$. Recently, another ADT mode (ADT$_{on–off}$), start-up/shut-down cycles, has gradually received attention.[63,64] The ADT$_{on–off}$ performed a linear potential sweep from 1.0 to 1.5 V vs. RHE for 20 000 cycles at a scan rate of 500 mV s^{-1} in an O$_2$-saturated 0.1 M HClO$_4$. After ADT$_s$, Pt_3Ni(Pt-skin)/Pd_{20}/C retained its ECSA and high activity (Fig. 5a and c), exhibiting only an ~2 mV shift for its $E_{1/2}$. This result is also consistent with the pioneering work by Adzic's group in which the modification of Pt_{nano} surfaces with Au clusters through UPD-Gal improved the stability of catalysts.[7] Our previous studies also demonstrated that nonspecific noble metal cluster (Pt, Pd or Au) modification through UPD-Gal enhanced the interaction between Pt_{nano} and the carbon support to improve catalyst durability during ADT$_s$.[11] Interestingly, Pt_3Ni(Pt-skin)/Pd_{20}/C shows the highest durability during ADT$_{on–off}$ (Fig. 5b and d). In the ADT$_{on–off}$, Pt dissolution and Ni leaching were serious issues for typical Pt/C or PtNi catalysts owing to their operation at a higher anodic potential. The superior stability of Pt_3Ni(Pt-skin)/Pd_{20}/C during the ADT$_{on–off}$ may be a result of the perfect Pt_3Ni(Pt-skin) structure. The Pt-skin located on the exterior of the PtNi shell effectively inhibits the dissolution of the Pd core and interior Ni sublayer leaching. The issue of Pt dissolution may have been improved due to the enlargement of the particle sizes of Pt_3Ni(Pt-skin)/Pd_{nano} in comparison with pristine Pd_{nano} (from ~5 nm to ~6.8 nm). It has previously been demonstrated that the Pt dissolution is significantly dependent on particle size and environmental acidity.[65] A larger particle size (>5 nm) could both reduce the trend of Pt dissolution and its activity. However, the ultra-thin layer Pt_3Ni(Pt-skin) modification not only stabilizes Pt from particle size enlargement but also significantly

Table 1 Performance of the Pt_3Ni(Pt-skin)/Pd_{20}/C catalyst and some representative results with high performance from recent published studies[a]

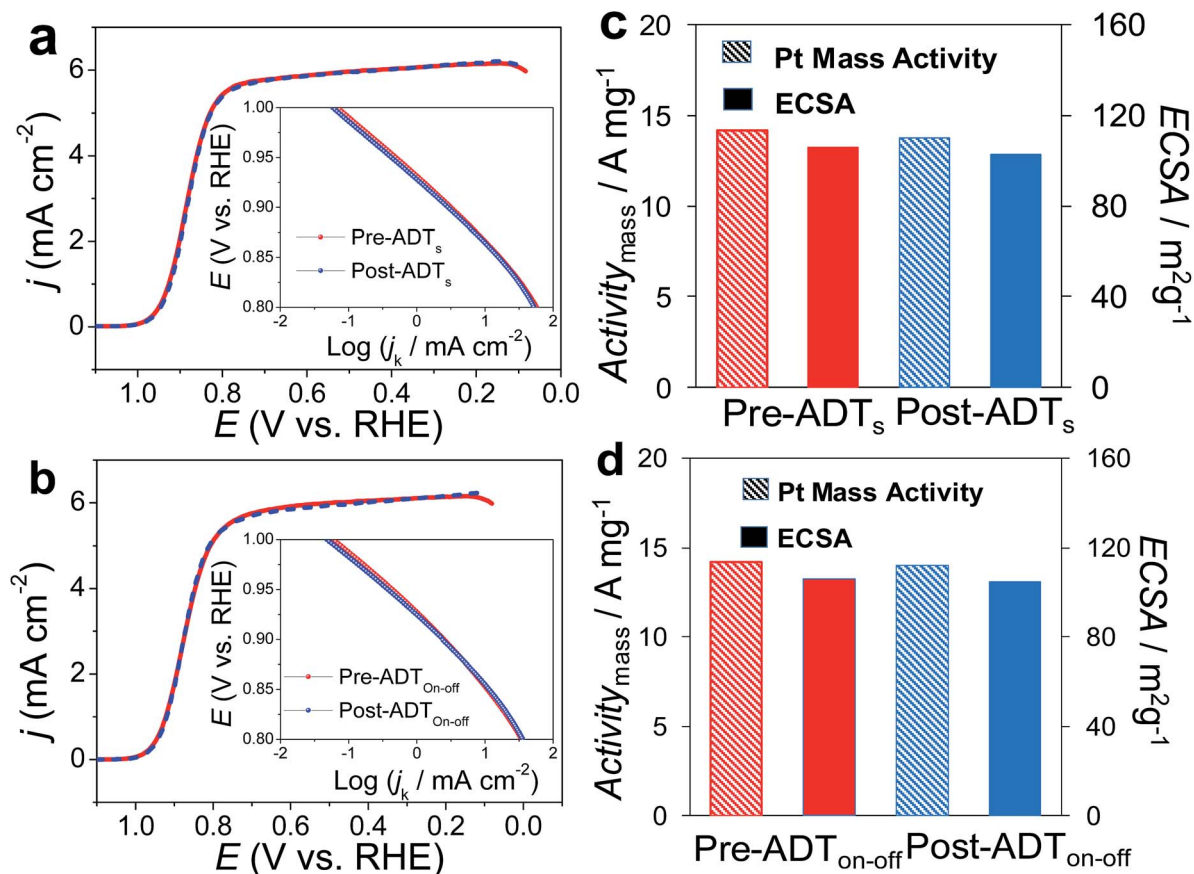| Catalysts	Pt loading (μg cm^{-2})	sECSA$_{CO}$ (m^2 g^{-1})	j_{kPt} (mA cm^{-2})	i_{mPt} (A mg$_{Pt}^{-1}$)	
Pt_3Ni(Pt-skin)/Pd_{20}/C	2.97	106	16.7	14.2	This work
Mo–Pt_3Ni/C	4.08	83.9	8.2	6.98	Ref. 62
Pt_3Ni/C nanoframes	N/A	N/A	1.48	5.7	Ref. 28
Jagged Pt nanowires	2.2	118	11.5	13.6	Ref. 31
Commercial Pt/C	24	91	0.185	0.091	This work

[a] N/A: not available.

Fig. 5 ORR polarization curves of the Pt₃Ni(Pt-skin)/Pd₂₀/C catalyst on a GC RDE (0.196 cm², ~2.97 µg cm⁻² Pt loading) (dashed line) before and (solid line) after accelerated durability tests include (a) ADT_s: a linear potential polarization from 0.6 to 1.0 V vs. RHE at a scan rate of 50 mV s⁻¹ for 20 000 cycles and (b) ADT_on-off: a linear potential polarization from 1.0 to 1.5 V vs. RHE for 20 000 cycles at a scan rate of 500 mV s⁻¹ in O₂-saturated 0.1 M HClO₄. Insets: the corresponding Tafel plots. (c) and (d) (solid pattern) sECSA_CO, and (slash pattern) Pt mass activities for (blue) before and (red) after accelerated durability tests.

enhances catalytic activity owing to the full exposure of Pt active sites on the surface of Pd/C.

Conclusions

In conclusion, considering that the Pt₃Ni(Pt-skin) structure exhibited the highest catalytic activity ever recorded, in this work, the challenge of preparing a nanocatalyst mimicking the Pt₃Ni(Pt-skin) structure was mitigated by growing a Ni_u covered Pd_nano core using the ZnUPD-Gal procedure. ZnUPD-Gal is an improvement to common CuUPD-Gal that offers more options of coating surfaces and facilitates more metal growth in the Gal process owing to the intrinsic lower Φ_{Zn} and more negative E^0 (Zn²⁺/Zn). The Pt₃Ni(Pt-skin) thin layer with ultra-low Pt loading presents not only a breakthrough in Pt specific activity and Pt mass activity, both of which were superior to those of state-of-the-art Pt–Ni catalysts, but also in high durability owing to the perfect Pt₃Ni(Pt-skin) construction.

Experimental

Chemicals

Carbon-supported palladium (Pd₂₀/C) (20 wt% Pd on XC-72 Valcan carbon (E-TEK)), Pt₂₀/C (20 wt% Pt on XC-72 Valcan

carbon (E-TEK)), 70% HClO₄ (JT-Baker), 95–98% H₂SO₄ (Aldrich), 98% NiSO₄·6H₂O (Aldrich), 98% Zn(ClO₄)₂·6H₂O (Aldrich), 99.7% Cu(NO₃)₂ (JT-Baker), 99.9% K₂PtCl₄ (Alfa), and 5% Nafion (NF) perfluorinated resin in a mixture of lower aliphatic alcohols and water (Aldrich) were used as received.

Electrochemical experiments

The electrochemical experiments were conducted using a CHI 760C potentiostat/galvanostat and a three-electrode electrochemical cell. To prevent Cl⁻ interference from the typical Ag/AgCl reference electrode, Hg/HgSO₄ (0.5 M H₂SO₄) was used as the reference electrode and Pt wire was used as the counter electrode. The potentials were measured against the reference electrode and converted to the reversible hydrogen electrode (RHE) reference scale by $E_{RHE} = E_{Hg/HgSO_4} + 0.68 + 0.059pH_{electrolyte}$. All potentials in this paper were stated with reference to the RHE. A glassy carbon (GC) electrode (Pine, 5.0 mm diameter, 0.196 cm² for the fabrication of electrocatalysts or the examination of electrocatalyst performance for the ORR) served as the substrate electrode for the Pd₂₀/C electrocatalyst suspension. The Pd₂₀/C catalyst suspension was prepared by mixing 10 mg of commercial Pd₂₀/C electrocatalyst powder in 5 mL of deionized water (with specific resistivity =

18.2 MΩ cm), followed by the gradual addition of 1 ml of iso-propyl alcohol and 20 min of ultrasonication to obtain a Pd_{20}/C suspension. The Pd_{20}/C@GC electrode was fabricated using a drop coating procedure. Briefly, a GC electrode was polished successively with 1.0, 0.3, and 0.05 µm alumina powder cloth (Buchler) followed by sonication in deionized water and drying prior to use. 2–7 µl of the Pd_{20}/C suspension was pipetted onto the surface of the GC electrode as a circle with a geometric area of 0.01–0.05 cm^2. Pd_{20}/C@GC was obtained after drying under an Ar flow at room temperature (∼28 °C) for solvent evaporation.

Preparation of Ni_u/Pd_{20}/C, $PtNi$/Pd_{20}/C, Pt_3Ni(Pt-skin)/Pd_{20}/C, Pt_3/Pd_{20}/C, and $(PtNi)_3$/Pd_{20}/C electrocatalysts

Pd_{20}/C@GCE was used as a working electrode to prepare relative catalysts. The microstructure of the post-modified Pd_{20}/C electrocatalysts was examined by the electrochemical characterization and image analysis. High-resolution transmission electron microscopy (TEM) images (HRTEM) and elemental composition micro-distribution of post-modified Pd_{20}/C electrocatalysts were obtained using a JEOL JEM-2100F field emission TEM (FE-TEM) equipped with an energy dispersive X-ray spectrometer (EDS).

Preparation of Ni_u/Pd_{20}/C. The Ni underpotential deposition (Ni_u) covered Pd_{20}/C@GC (Ni_u/Pd_{20}/C@GC) electrocatalyst was prepared by direct electrodeposition of Ni_u on the Pd surface of the Pd_{20}/C@GC electrode from a 0.5 M Na_2SO_4 aqueous solution (Na_2SO_{4aq}) containing 20 mM $NiSO_4$. The potential was stopped at −0.1 V vs. RHE for 20 min to allow the Ni_u to completely cover the entire Pd surface. All operations were carried out in a three-electrode electrochemical cell under an Ar atmosphere.

Preparation of $PtNi$/Pd_{20}/C. The Pt atomic layer was prepared by ZnUPD-Gal on the Ni surface of the as-prepared Ni_u/Pd_{20}/C@GC from 0.5 M Na_2SO_{4aq} containing 20 mM $Zn(ClO_4)_2$. The potential was stopped at 0.05 V vs. RHE for 10 min to allow the Zn_u to completely cover the whole surface of the Ni surface. All of these operations were carried out in a three-electrode electrochemical cell under an Ar atmosphere. The as-prepared Zn_u modified Ni_u/Pd_{20}/C@GC was rinsed with deionized water and immersed in a 0.2 M H_2SO_4 solution containing 1.0 mM K_2PtCl_4 for about 5 min to displace the Zn_u with Pt and to obtain Pt atomic layer modified Ni_u/Pd_{20}/C@GC ($PtNi$/Pd_{20}/C@GC).

Preparation of Pt_3Ni(Pt-skin)/Pd_{20}/C. The repetitive ZnUPD-Gal process was continually used to introduce the second and the third Pt atomic layers onto the as-prepared $PtNi$/Pd_{20}/C@GC to obtain Pt_3Ni(Pt-skin)/Pd_{20}/C@GC.

Preparation of Pt_3/Pd_{20}/C. The repetitive ZnUPD-Gal process continually introduced three Pt atomic layers on Pd_{20}/C@GC to obtain Pt_3/Pd_{20}/C@GC.

Preparation of $(PtNi)_3$/Pd_{20}/C. To extend the diversity of the ZnUPD-Gal on Ni_u, a Pt atomic layer and Ni_u repetitively overlapped shell, which was three repeated PtNi layers on a Pd core ($(PtNi)_3$/Pd_{20}/C), was prepared as a control example. Ni_u was electrodeposited on the Pt surface of the as-prepared $PtNi$/Pd_{20}/C@GC from 0.5 M Na_2SO_{4aq} containing 20 mM $NiSO_4$ (Ni_u/$PtNi$/Pd_{20}/C@GC) at a controlled potential of −0.05 V vs. RHE for

20 min to allow the Ni_u to completely cover the whole surface of the Pt surface. The Zn_u was electrodeposited on the as-prepared Ni_u/$PtNi$/Pd_{20}/C@GC from 0.5 M Na_2SO_{4aq} containing 20 mM $Zn(ClO_4)_2$, while controlling the potential at 0.05 V vs. RHE for 10 min. Subsequently, the Zn_u was replaced by more noble Pt in the GaI process, leading to Pt atomic layer covered Ni_u/$PtNi$/Pd_{20}/C@GC ($(PtNi)_2$/Pd_{20}/C@GC). The ZnUPD-GaI on Ni_u was used to introduce the third PtNi layer on $(PtNi)_2$/Pd_{20}/C@GC and obtain $(PtNi)_3$/Pd_{20}/C@GC.

Electrochemical characterization of the ORR

A commercial (Pine Instruments) rotating ring-disk electrode (RRDE) was used with a Pt ring and an interchangeable disk. The disk electrode was a GC rod modified by a thin layer of as-prepared electrocatalyst covered by a Nafion polymer thin film used as the working electrode for ORR measurements. The as-prepared working electrode was electrochemically cleaned using a cycling potential between 0.0 and 1.0 V (vs. RHE) 10 times in Ar-purged 0.1 M H_2SO_4, except for Ni_u/Pd_{20}/C owing to Ni_u leaching. The electrochemical surface areas (ECSA) of the electrocatalysts were determined by measuring the areas (charges) under the hydrogen adsorption peaks (H_{ad}) ($ECSA_H$) and the electro-oxidation of adsorbed carbon monoxide (CO_{ad}), otherwise known as CO stripping ($ECSA_{CO}$), respectively, in the cyclic voltammograms. A conversion factor of 0.21 mC cm^{-2} was used to determine $ECSA_H$. For CO stripping experiments, CO was adsorbed onto the pre-cleaned electrode by holding the potential at 0.05 V for 10 min in CO saturated 0.1 M $HClO_4$ solution. The CO stripping curve was taken after purging with Ar for 30 min. A conversion factor of 0.42 mC cm^{-2} was used to determine $ECSA_{CO}$. The specific ECSA values (sECSA = ECSA/metal loading, m^2 g^{-1}) of the electrocatalysts were evaluated from ECSAH ($sECSA_H$) and ECSACO ($sECSA_{CO}$). When considering the $ECSA_{CO}$ contribution from Pt ($ECSA_{CO(Pt)}$ = $sECSA_{CO}$ × the mass of Pt (∼2.97 µg$_{Pt}$ cm^{-2} for Pt_3Ni(Pt-skin)/Pd_{20}/C and Pt_3/Pd_{20}/C)), the Pt content was obtained by measuring the charge associated with Zn_u (after correcting for the double layer charging) on Pd_{20}/C and assuming that there was a one-to-one ratio between the UPD adlayer and Pt atoms. ORR experiments were performed in oxygen-saturated 0.1 M $HClO_4$ aqueous solution. The solution was purged for at least 30 min to ensure oxygen saturation. The ORR electrochemical experiments were conducted in a three-electrode electrochemical cell. Hg/HgSO$_4$ (0.5 M H_2SO_4) and a Pt wire were used as the reference and counter electrodes, respectively; however, all potentials are quoted with respect to a RHE. The scan rate was 0.01 V s^{-1}. A Pine Model AFMSR electrode rotator controlled the electrode rotation for the ORR electrochemical experiments. During measurement of the polarization curves for the ORR on the disk electrode, the Pt ring electrode was potentiostated at 1.1 V vs. RHE, a potential where the peroxide oxidation reaction is under pure diffusion control; the collection efficiency, N, for the ring-disk assembly was ∼0.2.

Accelerated durability test (ADT, linear potential scanning)

The durability of the Pt_3Ni(Pt-skin)/Pd_{20}/C catalyst was investigated in two ADT modes. In the ambient temperature potential

polarization, $Pt_3Ni(Pt\text{-}skin)/Pd_{20}/C@GC$ was used as the working electrode.

Accelerated durability tests related to catalyst lifetime (ADT_s). The ADTs were conducted by linear potential sweeping from 0.6 to 1.0 V vs. RHE at a scan rate of 50 mV s^{-1} for 20 000 cycles in an O_2-saturated 0.1 M $HClO_{4aq}$ at room temperature.

Accelerated durability test related start-up/shut-down cycles ($ADT_{on\text{-}off}$). The $ADT_{on\text{-}off}$ was conducted by linear potential sweeping from 1.0 to 1.5 V vs. RHE for 20 000 cycles at a scan rate of 500 mV s^{-1} in O_2-saturated 0.1 M $HClO_{4aq}$ at room temperature.

Conflicts of interest

There are no conflicts to declare.

Acknowledgements

Notes and references

1 I. E. L. Stephens, J. Rossmeisl and I. Chorkendorff, *Science*, 2016, **354**, 1378–1379.

2 M. H. Shao, Q. W. Chang, J. P. Dodelet and R. Chenitz, *Chem. Rev.*, 2016, **116**, 3594–3657.

3 M. K. Debe, *Nature*, 2012, **486**, 43–51.

4 L. Zhang, L. T. Roling, X. Wang, M. Vara, M. F. Chi, J. Y. Liu, S. I. Choi, J. Park, J. A. Herron, Z. X. Xie, M. Mavrikakis and Y. N. Xia, *Science*, 2015, **349**, 412–416.

5 Y. J. Wang, N. N. Zhao, B. Z. Fang, H. Li, X. T. T. Bi and H. J. Wang, *Chem. Rev.*, 2015, **115**, 3433–3467.

6 B. Lim, M. J. Jiang, P. H. C. Camargo, E. C. Cho, J. Tao, X. M. Lu, Y. M. Zhu and Y. N. Xia, *Science*, 2009, **324**, 1302–1305.

7 J. Zhang, K. Sasaki, E. Sutter and R. R. Adzic, *Science*, 2007, **315**, 220–222.

8 V. R. Stamenkovic, B. Fowler, B. S. Mun, G. F. Wang, P. N. Ross, C. A. Lucas and N. M. Markovic, *Science*, 2007, **315**, 493–497.

9 D. J. Berger, *Science*, 1999, **286**, 49.

10 J. F. Huang and W. Y. Chen, *Chem. Commun.*, 2015, **51**, 12052–12055.

11 J. F. Huang and H. Y. Hsiao, *ACS Appl. Mater. Interfaces*, 2016, **8**, 33749–33754.

12 J. F. Huang and H. W. Yang, *Anal. Chem.*, 2016, **88**, 6403–6409.

13 J.-F. Huang and W.-R. Chang, *J. Mater. Chem.*, 2012, **22**, 17961–17966.

14 F. Calle-Vallejo, M. D. Pohl, D. Reinisch, D. Loffreda, P. Sautet and A. S. Bandarenka, *Chem. Sci.*, 2017, **8**, 2283–2289.

15 A. Fortunelli, W. A. Goddard, L. Sementa, G. Barcaro, F. R. Negreiros and A. Jaramillo-Botero, *Chem. Sci.*, 2015, **6**, 3915–3925.

16 H. P. Liu, P. Zhong, K. Liu, L. Han, H. Q. Zheng, Y. D. Yin and C. B. Gao, *Chem. Sci.*, 2018, **9**, 398–404.

17 D. F. Yancey, L. Zhang, R. M. Crooks and G. Henkelman, *Chem. Sci.*, 2012, **3**, 1033–1040.

18 J. F. Huang and H. Y. Chen, *Angew. Chem., Int. Ed.*, 2012, **51**, 1684–1688.

19 M. K. Carpenter, T. E. Moylan, R. S. Kukreja, M. H. Atwan and M. M. Tessema, *J. Am. Chem. Soc.*, 2012, **134**, 8535–8542.

20 V. Stamenkovic, T. J. Schmidt, P. N. Ross and N. M. Markovic, *J. Phys. Chem. B*, 2002, **106**, 11970–11979.

21 L. Z. Bu, Q. Shao, E. Bin, J. Guo, J. L. Yao and X. Q. Huang, *J. Am. Chem. Soc.*, 2017, **139**, 9576–9582.

22 M. Zhou, H. L. Wang, M. Vara, Z. D. Hood, M. Luo, T. H. Yang, S. X. Bao, M. F. Chi, P. Xiao, Y. H. Zhang and Y. N. Xia, *J. Am. Chem. Soc.*, 2016, **138**, 12263–12270.

23 N. Becknell, Y. J. Kang, C. Chen, J. Resasco, N. Kornienko, J. H. Guo, N. M. Markovic, G. A. Somorjai, V. R. Stamenkovic and P. D. Yang, *J. Am. Chem. Soc.*, 2015, **137**, 15817–15824.

24 K. A. Kuttiyiel, Y. Choi, K. Sasaki, D. Su, S. M. Hwang, S. D. Yim, T. H. Yang, G. G. Park and R. R. Adzic, *Nano Energy*, 2016, **29**, 261–267.

25 H. Yang, *Angew. Chem., Int. Ed.*, 2011, **50**, 2674–2676.

26 L. Gan, M. Heggen, R. O'Malley, B. Theobald and P. Strasser, *Nano Lett.*, 2013, **13**, 1131–1138.

27 P. Strasser, S. Koh, T. Anniyev, J. Greeley, K. More, C. F. Yu, Z. C. Liu, S. Kaya, D. Nordlund, H. Ogasawara, M. F. Toney and A. Nilsson, *Nat. Chem.*, 2010, **2**, 454–460.

28 C. Chen, Y. J. Kang, Z. Y. Huo, Z. W. Zhu, W. Y. Huang, H. L. L. Xin, J. D. Snyder, D. G. Li, J. A. Herron, M. Mavrikakis, M. F. Chi, K. L. More, Y. D. Li, N. M. Markovic, G. A. Somorjai, P. D. Yang and V. R. Stamenkovic, *Science*, 2014, **343**, 1339–1343.

29 C. H. Cui, L. Gan, H. H. Li, S. H. Yu, M. Heggen and P. Strasser, *Nano Lett.*, 2012, **12**, 5885–5889.

30 L. Cao and T. Mueller, *J. Phys. Chem. C*, 2015, **119**, 17735–17747.

31 M. F. Li, Z. P. Zhao, T. Cheng, A. Fortunelli, C. Y. Chen, R. Yu, Q. H. Zhang, L. Gu, B. V. Merinov, Z. Y. Lin, E. B. Zhu, T. Yu, Q. Y. Jia, J. H. Guo, L. Zhang, W. A. Goddard, Y. Huang and X. F. Duan, *Science*, 2016, **354**, 1414–1419.

32 S. H. Zhou, B. Varughese, B. Eichhorn, G. Jackson and K. McIlwrath, *Angew. Chem., Int. Ed.*, 2005, **44**, 4539–4543.

33 D. Zhao and B. Q. Xu, *Angew. Chem., Int. Ed.*, 2006, **45**, 4955–4959.

34 K. Sasaki, J. X. Wang, H. Naohara, N. Marinkovic, K. More, H. Inada and R. R. Adzic, *Electrochim. Acta*, 2010, **55**, 2645–2652.

35 R. G. Chaudhuri and S. Paria, *Chem. Rev.*, 2012, **112**, 2373–2433.

36 K. A. Kuttiyiel, K. Sasaki, Y. M. Choi, D. Su, P. Liu and R. R. Adzic, *Nano Lett.*, 2012, **12**, 6266–6271.

37 M. B. Gawande, A. Goswami, T. Asefa, H. Z. Guo, A. V. Biradar, D. L. Peng, R. Zboril and R. S. Varma, *Chem. Soc. Rev.*, 2015, **44**, 7540–7590.

38 S. I. Choi, M. H. Shao, N. Lu, A. Ruditskiy, H. C. Peng, J. Park, S. Guerrero, J. G. Wang, M. J. Kim and Y. N. Xia, *ACS Nano*, 2014, **8**, 10363–10371.

39 R. R. Adzic, J. Zhang, K. Sasaki, M. B. Vukmirovic, M. Shao, J. X. Wang, A. U. Nilekar, M. Mavrikakis, J. A. Valerio and F. Uribe, *Top. Catal.*, 2007, **46**, 249–262.

40 M. B. Vukmirovic, J. Zhang, K. Sasaki, A. U. Nilekar, F. Uribe, M. Mavrikakis and R. R. Adzic, *Electrochim. Acta*, 2007, **52**, 2257–2263.

41 C. Koenigsmann, A. C. Santulli, K. P. Gong, M. B. Vukmirovic, W. P. Zhou, E. Sutter, S. S. Wong and R. R. Adzic, *J. Am. Chem. Soc.*, 2011, **133**, 9783–9795.

42 S. Trasatti, *J. Electroanal. Chem.*, 1971, **33**, 351–377.

43 D. M. Kolb, M. Przasnyski and H. Gerischer, *J. Electroanal. Chem.*, 1974, **54**, 25–38.

44 V. R. Stamenkovic, B. S. Mun, K. J. J. Mayrhofer, P. N. Ross and N. M. Markovic, *J. Am. Chem. Soc.*, 2006, **128**, 8813–8819.

45 C. Wang, M. F. Chi, D. G. Li, D. Strmcnik, D. van der Vliett, G. F. Wang, V. Komanicky, K. C. Chang, A. P. Paulikas, D. Tripkovic, J. Pearson, K. L. More, N. M. Markovic and V. R. Stamenkovic, *J. Am. Chem. Soc.*, 2011, **133**, 14396–14403.

46 C. H. Cui, L. Gan, M. Heggen, S. Rudi and P. Strasser, *Nat. Mater.*, 2013, **12**, 765–771.

47 S. J. Guo, D. G. Li, H. Y. Zhu, S. Zhang, N. M. Markovic, V. R. Stamenkovic and S. H. Sun, *Angew. Chem., Int. Ed.*, 2013, **52**, 3465–3468.

48 T. Fu, J. Fang, C. S. Wang and J. B. Zhao, *J. Mater. Chem. A*, 2016, **4**, 8803–8811.

49 S. Mezzavilla, C. Baldizzonev, A. C. Swertz, N. Hodnik, E. Pizzutilo, G. Polymeros, G. P. Keeley, J. Knossalla, M. Heggen, K. J. J. Mayrhofer and F. Schuth, *ACS Catal.*, 2016, **6**, 8058–8068.

50 X. Zhao, S. Takao, K. Higashi, T. Kaneko, G. Samjeske, O. Sekizawa, T. Sakata, Y. Yoshida, T. Uruga and Y. Iwasawa, *ACS Catal.*, 2017, **7**, 4642–4654.

51 B. W. Gregory and J. L. Stickney, *J. Electroanal. Chem.*, 1991, **300**, 543–561.

52 Y. G. Kim, J. Y. Kim, D. Vairavapandian and J. L. Stickney, *J. Phys. Chem. B*, 2006, **110**, 17998–18006.

53 J. R. Rumble, *CRC Handbook of Chemistry and Physics*, CRC Press, 98th edn, 2017.

54 M. D. Quaiyyum, A. Aramata, S. Moniwa, S. Taguchi and M. Enyo, *J. Electroanal. Chem.*, 1994, **373**, 61–66.

55 D. F. van der Vliet, C. Wang, D. G. Li, A. P. Paulikas, J. Greeley, R. B. Rankin, D. Strmcnik, D. Tripkovic, N. M. Markovic and V. R. Stamenkovic, *Angew. Chem., Int. Ed.*, 2012, **51**, 3139–3142.

56 A. J. Bard and L. R. Faulkner, *Electrochemical Method: Fundamentals and Applications*, John Wiley & Son, New York, 2nd edn, 2001.

57 M. H. Shao, J. H. Odell, S. I. Choi and Y. N. Xia, *Electrochem. Commun.*, 2013, **31**, 46–48.

58 B. Alvarez, V. Climent, A. Rodes and J. M. Feliu, *J. Electroanal. Chem.*, 2001, **497**, 125–138.

59 Y. Garsany, O. A. Baturina, K. E. Swider-Lyons and S. S. Kocha, *Anal. Chem.*, 2010, **82**, 6321–6328.

60 U. A. Paulus, A. Wokaun, G. G. Scherer, T. J. Schmidt, V. Stamenkovic, N. M. Markovic and P. N. Ross, *Electrochim. Acta*, 2002, **47**, 3787–3798.

61 U. A. Paulus, A. Wokaun, G. G. Scherer, T. J. Schmidt, V. Stamenkovic, V. Radmilovic, N. M. Markovic and P. N. Ross, *J. Phys. Chem. B*, 2002, **106**, 4181–4191.

62 X. Q. Huang, Z. P. Zhao, L. Cao, Y. Chen, E. B. Zhu, Z. Y. Lin, M. F. Li, A. M. Yan, A. Zettl, Y. M. Wang, X. F. Duan, T. Mueller and Y. Huang, *Science*, 2015, **348**, 1230–1234.

63 H. Schmies, A. Bergmann, J. Drnec, G. X. Wang, D. Teschner, S. Kuhl, D. J. S. Sandbeck, S. Cherevko, M. Gocyla, M. Shviro, M. Heggen, V. Ramani, R. E. Dunin-Borkowski, K. J. J. Mayrhofer and P. Strasser, *Adv. Energy Mater.*, 2018, **8**, 13.

64 K. Higashi, G. Samjeske, S. Takao, T. Kaneko, O. Sekizawa, T. Uruga and Y. Iwasawa, *J. Phys. Chem. C*, 2017, **121**, 22164–22177.

65 L. Tang, B. Han, K. Persson, C. Friesen, T. He, K. Sieradzki and G. Ceder, *J. Am. Chem. Soc.*, 2010, **132**, 596–600.